

On Thermalization in A Nonlinear Variant of the Discrete NLS Equation

Yagmur Kati,^{1,*} Aleksandra Maluckov,² Ana Mancic,³ and Panayotis Kevrekidis^{4,5}

¹*Department of Physics, Humboldt University of Berlin, Berlin, Germany*

²*Vinča Institute of Nuclear Sciences, National Institute of Republic of Serbia, POB. 522, 11001 Belgrade, Serbia*

³*Faculty of Sciences and Mathematics, University of Niš, Višegradska 33, 18000 Niš, Serbia*

⁴*Department of Mathematics & Statistics, University of Massachusetts Amherst, Amherst, Massachusetts, USA*

⁵*Department of Physics, University of Massachusetts Amherst, Amherst, Massachusetts, USA*

We study the thermalization properties of a fully nonlinear lattice model originally derived from the two-dimensional cubic defocusing nonlinear Schrödinger equation (NLS) using analytical and numerical methods. Our analysis reveals both ergodic and nonergodic regimes; importantly, we find broad parameter ranges where the dynamics is ergodic even though it lies outside the Gibbsian parameter regime (for both $D = 0.25$ and $D = 2$), and a higher-energy range where ergodicity breaks down. We observe that in a certain range of parameters, the system requires non-standard statistical descriptions, indicating a breakdown of conventional thermalization. We examine the influence of the nonlinear dispersion parameter D on the system's behavior, showing that increasing D enhances fluctuations and speeds up the crossover of $q(T)$ toward the $\sim 1/T$ scaling. By analyzing excursion times, probability density functions, and localization patterns, we characterize transitions between ergodic and nonergodic behavior. In long-time numerical simulations within the non-ergodic regime for $D > 1$, stable localization over two sites is observed, while $D < 1$ favors single-site localization in the high energy density regimes. Our results provide insights into the interplay between thermalization, localization, and non-standard statistical behavior in genuinely nonlinear systems.

I. INTRODUCTION

Nonlinear dispersive lattice models have emerged as an important modeling platform for a wide variety of physical settings. These range from optical waveguide arrays [1] to mean-field atomic condensates in optical lattices [2] and from granular crystals [3, 4] and cantilever arrays [5] to nonlinear electrical circuits [6] and biophysical settings such as the DNA double strand [7, 8]. This diverse set of experimental applications and the associated theoretical and computational tools associated with this field have by now been summarized in numerous reviews [9, 10], as well as books [6, 8, 11].

Among the relevant models, arguably the most prototypical one, operating as an envelope model broadly applicable (through appropriate reductions) to most of the above applications, one can mention the discrete nonlinear Schrödinger (DNLS) equation [12–14]. The DNLS model combines the principal ingredients of dispersive nearest-neighbor lattice dynamics and onsite (cubic) nonlinearity and as such is central to applications, e.g., in nonlinear optics of waveguide arrays [1], as well as to tunneling-coupled Bose-Einstein condensates at the wells of an optical lattice [2] [a topic that remains extremely active, including in experiments, to this day [15]]. The model supports a large variety of solitary waves that have been extensively analyzed in one spatial dimension, while more exotic vortical states exist in higher dimensional settings [14].

The study of thermalization and localization in nonlinear dynamical lattices is crucial for understanding a wide

range of physical phenomena, from energy transport in condensed matter to wave dynamics in optical lattices; after all this was fundamental in the original query of E. Fermi that led to the Fermi-Pasta-Ulam-Tsingou model and the birth of nonlinear science [16, 17]. In the context of the more standard DNLS model, this type of query has been considered in a substantial volume of publications following [18]. Nevertheless, relevant studies focusing on ergodicity properties and on energy localization, developing different types of diagnostics as well as exploring a diverse array of systems, are still a highly active area of research [19–25], including through the development of the so-called “optical thermodynamics” of weakly nonlinear lattices [26–28]. The study of the related possibility of reaching negative temperatures has recently been reviewed in [29] and the associated interpretation of localization as a form of condensation continues to be a topic of ongoing investigation [30].

Recently, a different class of DNLS models has emerged in a completely different setting. In the work of the so-called I-team a reduction from the two-dimensional defocusing cubic nonlinear Schrödinger equation on the torus [31, 32] led to a lattice model intended as a toy representation of turbulent cascades. Indeed, in this model the notion of a “lattice node” can be thought of as representing a group of wavenumbers in the Fourier space. Thus, potential mobility within this model could be thought of as representing the transfer of energy across frequencies. Among the intriguing features of this model one can list the fact that it is genuinely nonlinear (i.e., there is no linear dispersive part) and that it can thus support compactly supported nonlinear excitations [33]. The intrinsic interest within this type of setting led to studies of its numerical features [32], of

* yagmur.kati@hu-berlin.de

numerical schemes to integrate such models [34] and of its connections to solutions of a discrete Burgers equation [35].

The present work lies at the nexus of all these intriguing, ongoing themes of research. It extends the study of the thermodynamics of the DNLS [18, 20] and of the recent attempt [36] to go beyond the DNLS and towards approaching the integrable Ablowitz–Ladik analogue thereof [13], with these works involving subsets of the present authors, through the thermodynamics of the so-called Salerno model [37]. It connects this “thermodynamics of nonlinear lattice models” thread of research via the key transfer integral methodology of [38] with the setting of genuinely nonlinear models such as the one of [31], which no longer features solitary waves and regular discrete breathers, but rather focuses the energy on discrete compacton states [39, 40]. This is also emerging as a challenging frontier of statistical mechanics research efforts of nonlinear lattices, as is evidenced by the recent work of [41], aiming to construct the invariant measure of this lattice through a characterization of its energy minimizers.

The scope of the present study is to advance the current understanding of thermalization in nonlinear lattice models by providing insights into the intricate interplay between (genuine) nonlinearity, (compact) localization, and ergodicity as they emerge in the intriguing toy model of the I-team [31]. Our presentation is structured as follows. In section II we introduce the model of interest, outline the relevant conservation laws, and describe the thermodynamic formalism based on the transfer integral. We use section III to develop a series of tools that will be used in the computational analysis of the toy model, including finite time (mass or l^2 norm) averages, and probability density functions (PDFs) of so-called excursion times, i.e., some of the tools developed recently to explore the dynamics and thermodynamics of such lattice systems [20–22, 25]. In section IV we present a discussion of our findings. Finally, in section V, we summarize our conclusions, and offer an outlook towards possible future studies.

II. TOY MODEL SYSTEM & THERMODYNAMIC FORMALISM

The toy model of interest herein is derived from the nonlinear Schrödinger equation (NLS) on a two-dimensional toroidal domain with periodic boundary conditions. This setup facilitates the analysis of wave propagation and interaction effects. Colliander et al. [32] reduced the NLS to the toy model, described by the equations of motion:

$$i\dot{b}_\ell = |b_\ell|^2 b_\ell - D b_\ell^* (b_{\ell-1}^2 + b_{\ell+1}^2) \quad (1)$$

with boundary conditions $b_0 = b_{N+1} = 0$, where the over-dot represents the time derivative, ℓ is the site index, and

D is the parameter controlling the interaction between nearest neighbors. The equations of motion, given by

$$i\dot{b}_\ell = 2 \frac{\partial H}{\partial b_\ell^*} \quad (2)$$

define the system’s dynamics, where H is the Hamiltonian:

$$H = \sum_{\ell=1}^N \frac{1}{4} |b_\ell|^4 - \frac{D}{2} \operatorname{Re}(b_\ell^* b_{\ell-1}^2). \quad (3)$$

The dynamics of Eq. (1) conserve both the total energy H and the total norm $A = \sum_\ell |b_\ell|^2$. The two conserved quantities A and H give us a two-dimensional parameter space (a, h) to define our initial states, where $a = A/N$ is the norm density and $h = H/N$ is the energy density of the system.

To examine the system’s statistical properties, we define and determine the classical grand-canonical partition function Z following [18]; see also the pioneering work of [38]. We start with a canonical transformation, $b_\ell = \sqrt{A_\ell} e^{i\phi_\ell}$, which yields the Hamiltonian in the form:

$$H = \sum_{\ell=1}^N \frac{1}{4} |A_\ell|^2 - \frac{D}{2} A_\ell A_{\ell-1} \cos(2\phi_\ell - 2\phi_{\ell-1}). \quad (4)$$

This leads to the expression for the partition function in the grand-canonical ensemble:

$$Z = \int_0^\infty \int_0^{2\pi} \prod_{\ell=1}^N d\phi_\ell dA_\ell e^{-\beta(H+\alpha A)}, \quad (5)$$

where β is the inverse temperature and the Lagrange multiplier α serves as a chemical potential associated with the conservation of A . Integrating over the phase variable ϕ_ℓ , and symmetrizing the partition function we obtain:

$$Z = (2\pi)^N \int_0^\infty \prod_{\ell=1}^N dA_\ell I_0 \left[\frac{\beta D}{2} A_\ell A_{\ell-1} \right] \times \exp \left[\sum_{\ell=1}^N -\frac{\beta}{8} (A_\ell^2 + A_{\ell-1}^2) - \frac{\beta\alpha}{2} (A_\ell + A_{\ell-1}) \right]. \quad (6)$$

In the thermodynamic limit ($N \rightarrow \infty$), the integral in Z can be evaluated exactly by using the eigenvalues and eigenfunctions of the transfer integral operator (TIO) [18, 38, 42], a fundamental technique enabling such analysis for one-dimensional systems. In this limit, the partition function approximates as $Z \approx (2\pi\lambda_0)^N$, where λ_0 is the largest eigenvalue of the TIO [with exponentially small corrections associated with $\propto (\lambda_1/\lambda_0)^N$ where λ_1 is the next eigenvalue of the relevant operator], allowing us to compute the integral as:

$$\int_0^\infty dA_\ell \kappa(A_\ell, A_{\ell-1}) y(A_\ell) = \lambda y(A_{\ell-1}), \quad (7)$$

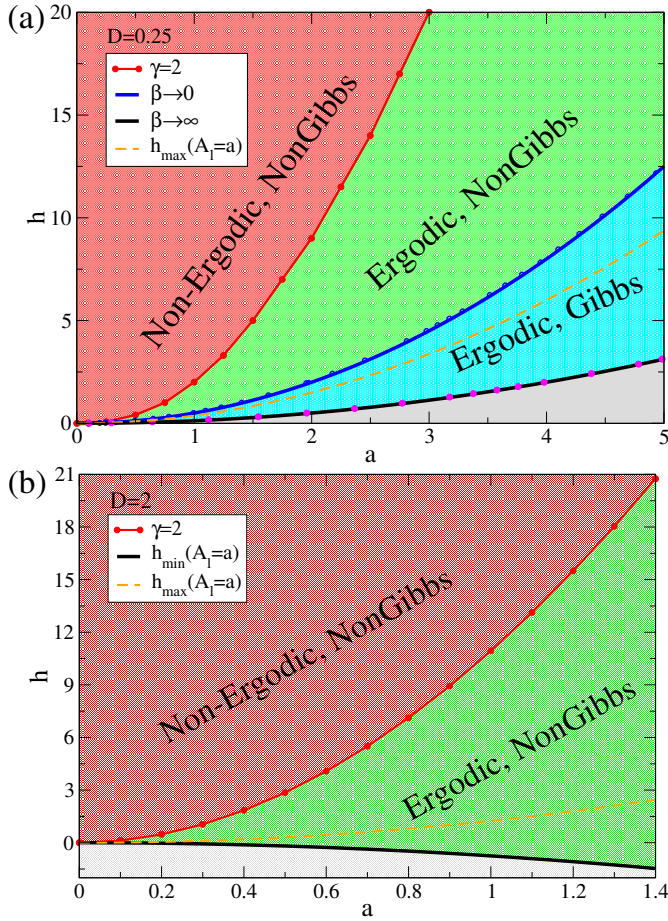


Figure 1. Phase diagram for the toy model with (a) $D = 0.25$ and (b) $D = 2$. In (a), the temperature curves for $\beta = 0$ and $\beta = \infty$ are given by $h = a^2/2$ (blue line, TIO blue circles) and $h = a^2/8$ (black line, TIO magenta circles), respectively. In both panels, red circles indicate initial states characterized by a decay exponent $\gamma = 2$ in the probability distribution of excursion times, marking the ergodic–nonergodic crossover. The orange dashed line shows the maximum energy achievable with a constant norm distribution, $h_{\max}(A_\ell = a) = \frac{a^2}{4}(1 + 2D)$. The black solid line, $h_{\min}(A_\ell = a) = \frac{a^2}{4}(1 - 2D)$, is the corresponding minimum for the initial states with a homogeneous norm and coincides with the ground state $h(\beta = \infty)$ for $D = 0.25$ in (a). In (b), this $h_{\min}(A_\ell = a)$ line is not the true ground state, as heterogeneous norm distributions allow energies that become unbounded from below in the thermodynamic limit for $D > 0.5$. While the TIO is only applicable in the cyan region of panel (a), each of the different regimes and their region of applicability are discussed in the text.

where the kernel matrix is

$$\kappa(x, z) = I_0 \left[\frac{D}{2} \beta x z \right] \exp \left[\sum_{\ell} -\frac{\beta}{8} (x^2 + z^2) - \frac{\beta \alpha}{2} (x + z) \right]. \quad (8)$$

Here x and z are continuous amplitude variables corresponding to two neighboring sites, $x \equiv A_\ell$ and $z \equiv A_{\ell-1}$, which are integrated from 0 to ∞ . In the context of Gibbs

thermodynamics, a well-defined temperature requires a non-divergent kernel matrix as $\beta \rightarrow 0$ and $\beta \rightarrow \infty$.

For values $D > 0.5$, however, the Kernel diverges, rendering the transfer integral method *inapplicable*. As D approaches 0.5, the Kernel assumes the asymptotic form:

$$\kappa(x, x) = \frac{\exp \left[-\frac{\beta x^2}{4}(1 - 2D) - \beta \alpha x \right]}{\sqrt{\pi D \beta x^2}}. \quad (9)$$

For $D > 0.5$ (and $\beta > 0$), the quadratic term changes sign and the exponent grows as $+\frac{\beta}{4}(2D - 1)x^2$, implying an exponential divergence of $\kappa(x, x)$ at large x . The case $D = 0.5$ is marginal: the quadratic term vanishes and $\kappa(x, x) \propto e^{-\beta \alpha x}/x$, so convergence requires $\beta \alpha > 0$ (in particular, $\alpha > 0$ for $\beta > 0$). Therefore, kernel convergence (and applicability of the transfer-integral method) is ensured for $D < 0.5$, and for $D = 0.5$ provided $\beta \alpha > 0$.

Since a valid Gibbs temperature curve in the parameter space (a, h) (see Fig.1) is not generally possible for $D > 0.5$, we at first consider the case $D = 0.25$ as representative (of the regime where thermalization—and associated computation via TIO—is possible) to start the investigation of the system relaxation. With the transfer integral method, an initial state in the parameter space (a, h) can correspond to the Gibbs parameters (β, α)

$$a = -\frac{1}{\beta \lambda_0} \frac{\partial \lambda_0}{\partial \alpha}, \quad h = -\frac{1}{\lambda_0} \frac{\partial \lambda_0}{\partial \beta} - \alpha a. \quad (10)$$

These equations are expected to provide a one-to-one mapping between the dynamical quantities of a given initial state (a, h) and the corresponding thermodynamic ones (β, α) of the thermalized asymptotic state, when thermalization is achieved.

We define the finite temperature region in the parameter space (a, h) to investigate the Gibbs regime, where the system thermalizes and its statistics is well-defined. By applying Eq. (10), we derive the infinite temperature line ($\beta = 0$) as $a = \frac{1}{\alpha \beta}$ and $h = \frac{1}{2\alpha^2 \beta^2} = \frac{a^2}{2}$ (See Appendix A). We can reach the ground state with a plane wave $b_\ell = \sqrt{a} e^{i\pi\ell/2}$ [18] that suggests a constant norm density distribution $A_\ell = a$. Inserting it into Eq.(4) gives

$$h = \frac{1}{4} a^2 - \frac{D}{2} a^2 \cos(2\Delta\phi), \quad (11)$$

where the phase difference $\Delta\phi = 0$ gives the zero temperature curve $h = \frac{1-2D}{4} a^2$ for $D < 0.5$. Similarly, the maximum energy density that would be reached with a constant norm is $h = \frac{1+2D}{4} a^2$, setting $\Delta\phi = \pi/2$ for all ϕ_ℓ . For our numerical results, we define the initial condition as follows.

$$b_\ell = \sqrt{A_\ell} e^{i\phi_\ell}, \quad (12)$$

where A_ℓ represents the amplitude and ϕ_ℓ the phase. In all simulations presented in this paper, we set the number of sites to $N = 1000$. When it is possible to define the initial condition by a constant norm i.e. $\frac{1-2D}{4} a^2 < h <$

$\frac{1+2D}{4}a^2$, we simply set $A_\ell = a + \delta_\ell$ and use a fixed phase difference with a small perturbation $\phi_\ell = \ell\Delta\phi + \delta'_\ell$, where

$$\Delta\phi = \frac{1}{2} \arccos \left[\frac{1}{2D} - \frac{2h}{Da^2} \right]. \quad (13)$$

Here, δ_ℓ and δ'_ℓ are two independent sets of random numbers which are uniformly distributed over $[-0.001, 0.001]$. We introduce them as a small disturbance to both A_ℓ and ϕ_ℓ for the numerical simulations.

Note that for $D = 0.5$, the infinite temperature line $h(\beta = 0)$ will correspond to the maximum energy density line reached by a constant norm, that is, $h_{\max}(A_\ell = a) = \frac{(1+2D)a^2}{4} = a^2/2$. Since a valid Gibbs temperature definition is only possible for $D \leq 0.5$, this correspondence implies that a nonconstant-amplitude distribution of lattice sites is necessary to test in the non-Gibbs parameter space (also called "negative temperatures"), where we expect to also find nonergodic states. It is relevant to mention here that, similarly to the standard DNLS, in the present case as well, it is natural to expect that there is a regime of (a, h) parameters beyond $\beta \rightarrow \infty$ where the regime is non-Gibbsian, yet one still expects thermalization, in line with, e.g., the work of [20]; in addition, for even higher energy/more nonlinear regimes, a nonergodic (and non-Gibbs) regime is expected to be identified where no observable thermalization takes place. In the present setting, densities with $h > (1+2D)a^2/4$ require a random amplitude distribution instead of a constant one. For $D = 0.25$ in Fig. 1, we show this region of densities above the orange dashed line $h = 3a^2/8$. We can prepare the associated initial states as

$$b_\ell = \sqrt{A_\ell} e^{i\pi\ell/2}, \quad A_\ell = a + \epsilon_\ell^c \exp[x\eta_\ell], \quad (14)$$

where ϵ_ℓ and η_ℓ are independent random variables, with ϵ_ℓ uniformly distributed in $[0, 1]$ and η_ℓ uniformly distributed in $[-1, 1]$. x and c are non-negative real numbers that control the energy density. Here we set $\Delta\phi$ to $\pi/2$, and a to the desired norm density, which is 0.25 for most of the plots shown in this paper.

As we just mentioned, a random seed is used for ϵ_ℓ, η_ℓ for each realization of the initial states with a high H/A^2 . Therefore, one may consider that an initial state with strongly excited two or more adjacent sites is also possible. Hence, we additionally prepare an atypical but probable initial state that is not used for average statistics such as the ones explained in the following sections III A and III B, but to test the existence and survival of several site compactons (dynamically relevant to this model in line also with the discussion of [33]), as described in section III C.

These compactly supported states are constructed as follows. After we prepare the high-energy initial state as in Eq.(14), we set $A_0 = \max(A_\ell)/m$, and then additionally excite m adjacent sites with the amplitude A_0/m in the middle of the lattice with $b_S = \sqrt{A_0} e^{i\phi_S}$ where $S = \{\ell_0, \dots, \ell_0 + m - 1\}$. We set $\phi_S = S\Delta\phi = S\pi/2$

unless it is a test run for the low-energy in-phase structures, where $\Delta\phi$ is set to zero. For $m = 2$, we choose $\ell_0 = N/2$, and for $m = 3$, $\ell_0 = N/2 - 1$. The initial state for the compacton tests can be described as follows

$$b_\ell = \sqrt{A_\ell} e^{i\pi\ell/2}, \quad A_\ell = a + \epsilon_\ell^c \exp[x\eta_\ell], \quad A_0 = \frac{\max(A_\ell)}{m}$$

$$b_S = \sqrt{A_0} e^{i\phi_S}, \quad S = \{\ell_0, \dots, \ell_0 + m - 1\}, \quad \ell \notin S. \quad (15)$$

In this manuscript, for the initial-states defined by Eq. (15), we will share norm density pictures only for $m = 2$ and $m = 3$. Note that we also tested several adjacent excited-site cases with $m = 4, \dots, 14$; however, these multi-site structures ($m > 3$) did not survive to later stages of the evolution, nor did they form spontaneously later. Instead, they rapidly converged to one, two or three site moving structures (the transition is not shown here, see Appendix B for analytical reasoning).

For all initial conditions described above, to maintain the desired average norm density a , we normalize the lattice by first calculating the current total norm A_c , then rescale each b_ℓ by $b_\ell \rightarrow b_\ell \sqrt{aN/A_c}$ such that $\sum_{\ell=1}^N |b_\ell|^2 = aN$.

Fig. 1 shows the phase diagrams of energy density h versus norm density a for $D = 0.25$ and $D = 2$. According to equilibrium statistical mechanics [43, 44] the Hamiltonian has to be bounded from below to have a convergent partition function. In both panels, the solid black line represents the minimum energy reached by a constant norm density, $h_{\min}(a_\ell = a) = \frac{a^2}{4}(1 - 2D)$ (see Eq. (A25) for details). For $D = 0.25 < 0.5$, this curve is convex and corresponds to the true ground-state line, meaning it is size-independent and the region below is inaccessible to any initial state. For $D = 2$, the same equation becomes concave and no longer represents the ground state. In this case, by heterogeneously redistributing the norm, the energy can be reduced up to $h_{\min}(a) = -7a^2N/44$ (see Eq. (26) below). The latter is the minimum for $D = 2$ [33] that is reached by only exciting three sites with $A_\ell = A_{\ell+2} = 3, A_{\ell+1} = 5$ (for $D = 2$, the minimum energy is achieved with exciting only nearest three sites with a 3-5-3 proportionality of the respective square moduli) and normalizing the lattice to have the desired a , as described in the previous paragraph. In the thermodynamic limit $N \rightarrow \infty$, the minimum energy density becomes unbounded from below, and no global ground-state line exists. Hence, note that the gray area in Fig 1(b) is accessible and non-Gibbs thermalizable in its nature, while the gray area in Fig.1(a) is inaccessible.

Our main conclusions from the results of Fig. 1 are then the following. In the regime where TIO is applicable ($D \leq 0.5$), we expect the system to thermalize, i.e., to reach thermodynamic equilibrium with a given temperature (between 0 and ∞) and chemical potential for a given pair of (a, h) . Going beyond the infinite temperature limit, we enter a regime of negative temperatures within the system (still for $D \leq 0.5$). That regime can be partitioned to a region (denoted by green color) where

thermalization still takes place but cannot be described by a Gibbs-type TIO approach in this regime of negative temperatures. Deeper into the nonlinear regime of red-coloring within the (a, h) plane, our diagnostics developed below suggest a nonergodic, non-Gibbs regime manifesting persistent localization. On the other hand, remarkably in the case of $D = 2$, there is no region of TIO applicability and Gibbs-thermalization, for the reasons discussed above. Here, in the (a, h) plane regions that we have accessed, we have only been able to identify a thermalization regime of negative temperature (denoted by the green color). Finally, in the red region, once again for $D = 2$, localization dominates the dynamics and prevents full thermalization on the simulated time scales.

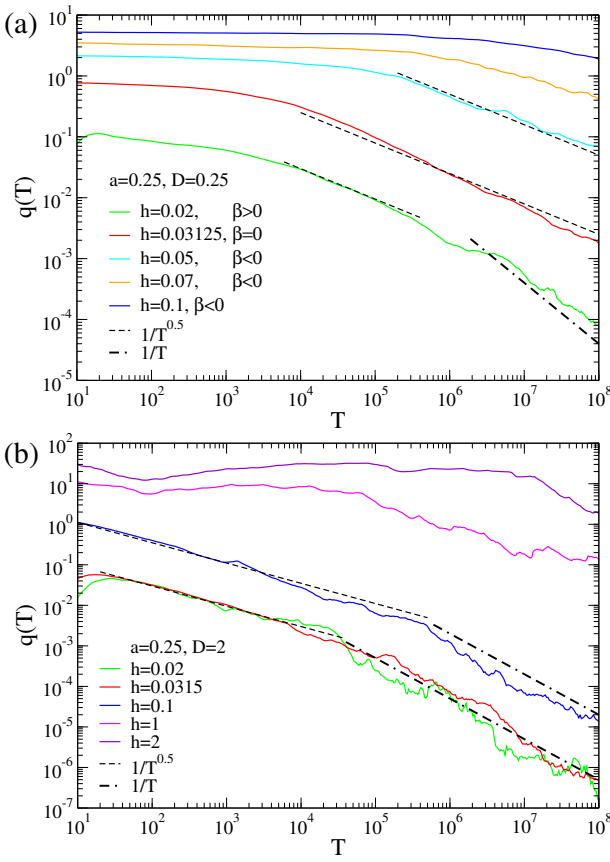


Figure 2. Finite time averages $q(T)$ for $a = 0.25$ with (a) $D = 0.25$ for $h = 0.02, 0.03125, 0.05, 0.07, 0.1$, and (b) $D = 2$ for $h = 0.02, 0.03125, 0.1, 1, 2$.

III. THERMALIZATION & DYNAMICAL LOCALIZATION: DIAGNOSTICS AND RESULTS

In this section, we explain the methods that we used to analyze the thermalization of the toy model. Section III A describes the so-called finite-time averages method in detail. This method examines the variance between the ensemble and the time averages of the observables

$|b_\ell|^2$, in this way gauging the potential ergodicity of the system. Section III B explains how we study the probability density function of the excursion times of the trajectories of observables off the equilibrium manifold (their ensemble average a).

Third, we study the stability and occurrence of few-site stable localizations in the nonergodic regime of different interaction strengths of D . Assuming a high amplitude few site structure has neighboring sites with amplitudes much smaller than itself, we follow the compacton analysis described in [33]. We then obtain the pictures of the norm density per site in time $a_\ell(t)$, to confirm if this analytical estimation for compactons is valid and possible for randomized initial states in a large lattice.

In all simulations, we integrated the equations of motion (1) with an explicit adaptive Dormand–Prince Runge–Kutta scheme of order 8(7) (DOPRI8, using an embedded error estimator for step-size control). We set $dt = 0.1$ as the maximum step size (with the initial trial step size dt/n_s); then the integrator adaptively adjusted the internal step size to satisfy the tolerance. We kept the relative norm error $|A(t) - A(0)|/A(0)$ below 10^{-10} and the relative energy error $|H(t) - H(0)|/H(0)$ below 10^{-8} , where $A(t)$ and $H(t)$ are the total norm and total energy at time t , respectively. For our results in this paper, the CPU time to reach $t = 10^8$ ranges from 4 days to 4 weeks depending on D and the selected densities a, h . It decreases as D, a , and h are reduced.

A. Finite Time Averages

We measure the dimensionless variance $q(T)$ over time to evaluate the system's thermalization by considering the local norm (mass) densities $|b_\ell|^2$ as time-dependent observables. Finite-time averages for $q(T)$ are defined as:

$$q(T) = \frac{m_2(T)}{m_1^2(T)}, \quad (16)$$

where

$$m_1(T) = \frac{1}{N} \sum_{\ell=1}^N \frac{1}{T} \int_0^T |b_\ell(t)|^2 dt, \quad \text{and} \quad (17)$$

$$m_2(T) = \frac{1}{N} \sum_{\ell=1}^N \left[\frac{1}{T} \int_0^T |b_\ell(t)|^2 dt - m_1 \right]^2. \quad (18)$$

In thermalized (ergodic) regimes, time and ensemble averages converge and $q(T)$ decays toward zero. For $D < 0.5$, where β is well-defined, we can probe both Gibbs and non-Gibbs regimes. For $D = 0.25$ we find that thermalized cases typically show an initial $\sim 1/\sqrt{T}$ power-law decay before ultimately reaching $\sim 1/T$, as expected for ergodic dynamics [21, 25].

Fig. 2 illustrates this power-law approach of $q(T)$ to zero in thermalizing systems, with deviations from this trend in some high-energy cases that appear nonergodic.

For $h = 0.02$ (green) in Fig. 2(a) and $h = 0.1, 0.03125, 0.1$ (green, red, blue) in Fig. 2(b), we observe an initial decay $q(T) \sim 1/\sqrt{T}$, followed at longer times by a faster $\sim 1/T$ scaling. For $h = 0.03125$ (red) and $h = 0.05$ (cyan) in Fig. 2(a), only the $\sim 1/\sqrt{T}$ regime is visible within our time window. A $\sim 1/\sqrt{T}$ regime followed by a faster $\sim 1/T$ decay was also reported for a finite-size nonlinear unitary-circuit lattice model [25]. In our simulations, the duration of the intermediate $\sim 1/\sqrt{T}$ regime depends on the initial state and, for fixed a , D , and N , generally increases with the average energy density. For larger h , initial states with $h = 0.07, 0.1$ (orange, blue) in Fig. 2(a) and $h = 1, 2$ (magenta, purple) in Fig. 2(b) exhibit a slower decay of the variance with no clear asymptotic scaling, suggesting nonergodic dynamics. To confirm whether the system is ergodic or not, we also study the probability density function of excursion times, as described in the next section III B.

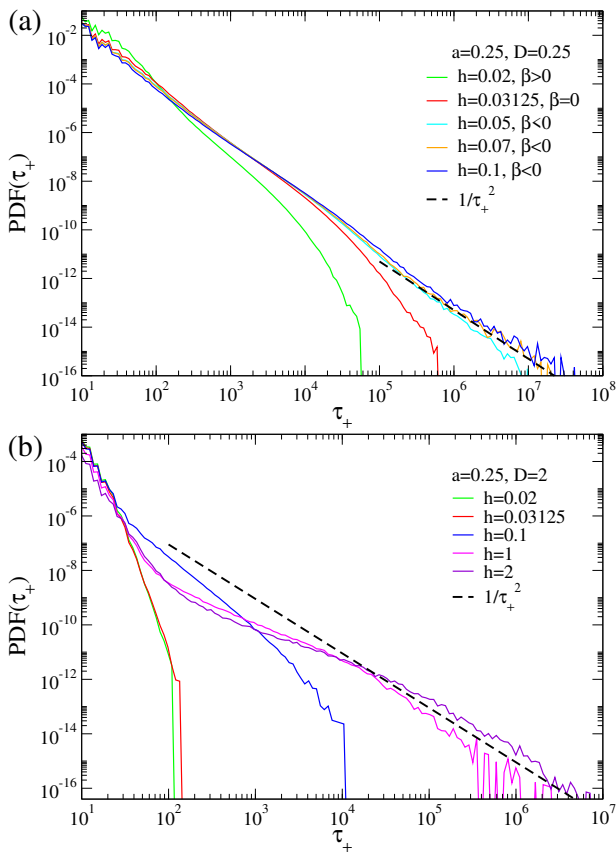


Figure 3. The probability density function of the initial states for $a = 0.25$ with (a) $D = 0.25$, (b) $D = 2$ for different energy densities h . The black dashed lines in both panels refer to a power law decay with an exponent $\gamma = 2$ ($\sim 1/\tau_+^2$), to point out the results that has $\gamma \leq 2$ (nonergodic), and results that has $\gamma > 2$ (ergodic).

B. PDF of Excursion Times

As in the previous section, we choose the local norm densities, $a_\ell = |b_\ell|^2$, as our local observables. The diagnostic developed herein proceeds by calculating the mean norm density a for the entire system and then tracking each $a_\ell(t)$. We count the instances when $a_\ell(t)$ crosses the equilibrium value (or so-called the ensemble average of the observables $\langle a_\ell \rangle_\Gamma = a$) and measure the time intervals between these piercings, which are called *excursion times* [20, 45]. Specifically, we classify the excursion times τ based on whether $a_\ell > a$ or $a_\ell < a$, denoting them as τ_+ and τ_- , respectively. We then determine the probability distribution function (PDF) for τ_+ and τ_- . To compute the $PDF(\tau_\pm)$, we bin the values of τ_\pm and normalize by the total number of events.

The mean excursion time, in general, can be defined as

$$\langle \tau \rangle = \int_{\tau_0}^{\infty} \tau PDF(\tau) d\tau \sim \int_{\tau_0}^{\infty} \tau (1/\tau^\gamma) d\tau, \quad (19)$$

where $PDF(\tau)$ denotes either $PDF(\tau_+)$ or $PDF(\tau_-)$, $\tau_0 > 0$ is a lower cutoff (a minimal excursion time), and the power-law form is assumed for the tail of $PDF(\tau)$. If the power-law decay exponent $\gamma \leq 2$, the mean of τ diverges, which signifies infinitely large excursion times. Thus, we expect $\gamma \leq 2$ for a nonergodic system (see [20] for details).

While we compute both $PDF(\tau_+)$ and $PDF(\tau_-)$, we focus on $PDF(\tau_+)$ to examine the ergodic-to-nonergodic crossover, as in previous studies [20, 21]. This is because we are interested in how much time some trajectories of a_ℓ spend at higher densities ($a_\ell(t) > a$), which appear as localizations in time in the norm density dynamics.

In our simulations, the tails of $PDF(\tau_+)$ for initial states in the Gibbs regime ($\beta > 0$) consistently exhibit a power-law decay with exponent $\gamma > 2$. This implies finite mean excursion times and supports ergodic dynamics in the Gibbs regime. Such behavior is expected within Gibbs statistics and has been observed for other lattice models, including the DNLS [20], Klein–Gordon [22], and Josephson-junction chains [21]. An example is shown in Fig. 3(a) (and Fig. 2(a)) for $D = 0.25$, $a = 0.25$, and $h = 0.02$.

More interestingly, we also find $\gamma > 2$ for some initial states in the non-Gibbs regime ($\beta < 0$). A representative case ($a = 0.25$, $h = 0.05$) in the ergodic but non-Gibbs (green) region is shown in Fig. 2(a) and Fig. 3(a). We locate the ergodic–nonergodic crossover by scanning initial states in the (a, h) plane and identifying where the PDF method yields $\gamma = 2$. The resulting boundary (solid red line) in Fig. 1(a) does not coincide with the $\beta = 0$ line (blue), leaving a significant intermediate region (green) that is ergodic yet non-Gibbs. Similar thermalized but non-Gibbsian regions are known in other nonlinear lattice models such as DNLS [20] and Salerno [36].

Fixing the norm density at $a = 0.25$ and increasing the energy density h further into the $\beta < 0$ (non-Gibbs) part

of the density diagram, we eventually enter the nonergodic (red) region in Fig. 1. In this regime the excursion-time PDF develops a power-law tail with $\gamma \leq 2$ (orange and blue curves in Fig. 3(a)), implying diverging mean excursion times. This confirms that nonergodic dynamics can occur within the non-Gibbs regime, but it does not cover the entire $\beta < 0$ region.

In Fig. 3(b) we repeat the same initial-state construction as in Fig. 3(a), but now for $D = 2$. Using the same (a, h) values as in Fig. 3(a) (i.e., $0.02 \leq h \leq 0.1$, including the cases that are nonergodic for $D = 0.25$), we find $\gamma > 2$ for all these runs, indicating ergodic dynamics at $D = 2$. This suggests that the stronger nearest-neighbor interaction at larger D enhances chaos and promotes thermalization. To access nonergodic behavior at $D = 2$ we therefore increase the energy density further at fixed a , which leads to $\gamma \leq 2$ for $h = 1$ and $h = 2$ (Fig. 3(b)), consistent with the nonergodic (red) region in the (a, h) phase diagram of Fig. 1(b). In these high-energy cases, the system does not thermalize within our longest integration times, $t \leq 10^8$.

C. Mechanism for few-site localization

For the nonergodic regime, long-time integrations of Eqs. (1)–(3) show that the norm density $a_\ell = |b_\ell|^2$ becomes strongly localized: it concentrates on a single site for $D < 1$, and, typically, on two adjacent sites for $D > 1$. We verified this trend for $0.01 \leq D \leq 2$ (not shown).

A natural explanation comes from the standing-wave compactons supported on m sites ($m = 1, 2, 3$) analyzed in [32, 33]. These solutions assume that all sites outside the compact support are exactly zero, whereas our initial data excite the entire lattice. Nevertheless, at a high energy for fixed total norm (an initial state with a high H/A^2), the dynamics *spontaneously* concentrates a significant portion of the total norm on the block(s) of one or few adjacent sites, while the rest of the chain carries small-amplitude oscillations. In line also with the argumentation of [41], in regimes of *positive temperature*, one would expect this to single out *energy minimizers*, while in regimes of *negative temperature* to localize the mass into *energy maximizers*. Accordingly, in the non-ergodic regime, the compacton energies provide accurate local energetic guidance towards the localized profiles that should be observed in the long-time evolution of the system.

We therefore proceed to evaluate the Hamiltonian (3) on standing-wave compactons supported on m sites with compact support $S = \{\ell_0, \dots, \ell_0 + m - 1\}$ for $m = 1, 2, 3$, and $b_\ell = 0$ for $\ell \notin S$. On S we define

$$b_\ell = \sqrt{A_\ell} e^{i\phi_\ell}, \quad A_\ell \geq 0, \quad \sum_{\ell \in S} A_\ell = A.$$

Only adjacent sites within S enter the interaction term in (3), for each adjacent pair $(\ell, \ell - 1)$

$$\text{Re}[(\bar{b}_\ell)^2 b_{\ell-1}^2] = A_\ell A_{\ell-1} \cos(2(\phi_\ell - \phi_{\ell-1})).$$

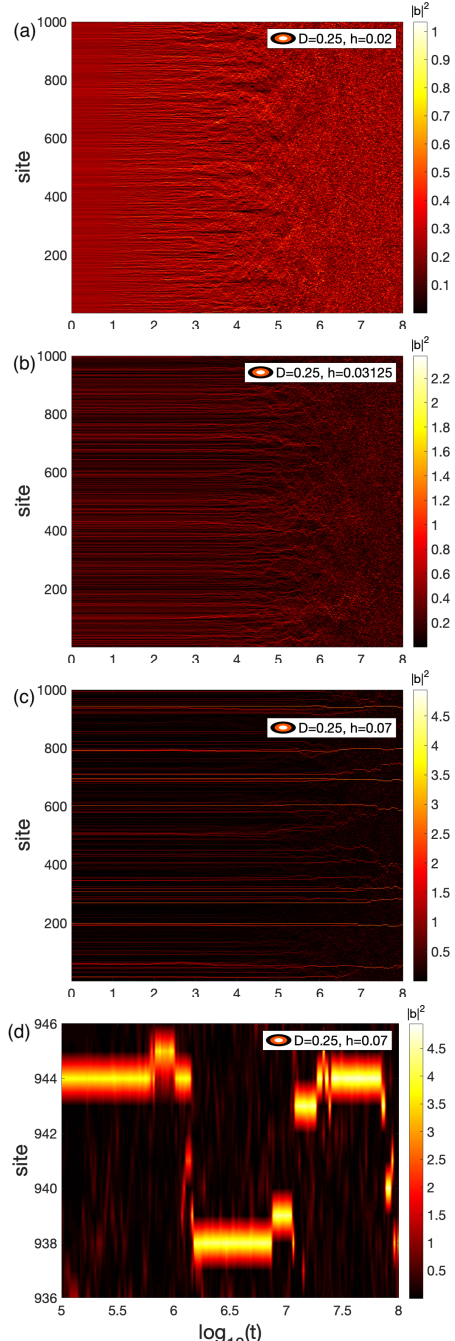


Figure 4. Increasing energy density reduces chaotic mixing and leads to long-lived localization at fixed $D = 0.25$ and $a = 0.25$. Local norm densities $a_\ell(t)$ are color coded in time for (a) $h = 0.02$ ($\beta > 0$), (b) $h = 0.03125$ ($\beta = 0$), and (c) $h = 0.07$ ($\beta < 0$). Part (d) shows a zoomed view of (c), where one-site localization persists for long times.

Following [33], we call $\phi_\ell - \phi_{\ell-1} = 0$ a real "in-phase" compacton and $\phi_\ell - \phi_{\ell-1} = \pi/2$ a "staggered" compacton. In this paper, we will focus more on the existence of staggered compactons on a lattice, as we investigate the nonergodic initial states with a high H/A^2 . The work of [33] examined energy minimizers earlier (see,

e.g., their Fig. 7) [see also the discussion of [41]], however, in our nonergodic regime of negative temperatures, it is the maximizers (which are often suitable staggered configurations) that become central to the dynamics.

1 site. $S = \{\ell_0\}$, $A_{\ell_0} = A$. There are no adjacent sites within the support, so the interaction term in (3) vanishes:

$$H_1 = \frac{1}{4} A^2 \quad (\text{independent of } D). \quad (20)$$

2 sites. $S = \{\ell_0, \ell_0 + 1\}$, set $A_{\ell_0} = x$, $A_{\ell_0+1} = y$ with $x + y = A$. Then

$$H(x, y) = \frac{1}{4}(x^2 + y^2) \mp \frac{D}{2}xy,$$

where the upper ($-$) sign corresponds to the in-phase (real) compacton ($\Delta\phi = 0, \cos(2\Delta\phi) = 1$) and the lower ($+$) sign to the staggered compacton ($\Delta\phi = \pi/2, \cos(2\Delta\phi) = -1$). Extremizing under $x + y = A$ (by symmetry or a Lagrange multiplier), per the results of Appendix B, gives $x = y = A/2$, hence

$$H_{2,\text{in}}(D) = \frac{1-D}{8} A^2, \quad H_{2,\text{stag}}(D) = \frac{1+D}{8} A^2. \quad (21)$$

3 sites. $S = \{\ell_0 - 1, \ell_0, \ell_0 + 1\}$, set $A_{\ell_0-1} = A_{\ell_0+1} = x$, $A_{\ell_0} = y$, with $2x + y = A$.

$$H(x, y) = \frac{1}{2}x^2 + \frac{1}{4}y^2 - Dxy \cos(2\Delta\phi)$$

For the staggered compacton ($\Delta\phi = \pi/2$), extremize

$$\mathcal{L}(x, y, \lambda) = \frac{1}{2}x^2 + \frac{1}{4}y^2 + Dxy + \lambda(2x + y - A),$$

which gives the stationarity system

$$\partial_x \mathcal{L} : \quad x + Dy + 2\lambda = 0, \quad (22)$$

$$\partial_y \mathcal{L} : \quad \frac{1}{2}y + Dx + \lambda = 0, \quad (23)$$

$$2x + y = A. \quad (24)$$

Solving yields

$$x = \frac{1-D}{3-4D} A, \quad y = \frac{1-2D}{3-4D} A \quad (D \neq \frac{3}{4}),$$

and the corresponding energy

$$H_{3,\text{stag}}(D) = \frac{1-2D^2}{4(3-4D)} A^2. \quad (25)$$

An analogous three-site calculation for the in-phase configuration ($\Delta\phi = 0$) yields

$$x = \frac{1+D}{4D+3} A, \quad y = \frac{1+2D}{4D+3} A,$$

and

$$H_{3,\text{in}}(D) = \frac{1-2D^2}{4(4D+3)} A^2, \quad (26)$$

so that for $D = 2$ one finds $H_{3,\text{in}} = -7A^2/44$, which is the global minimum at fixed A ; cf. also the associated discussions of [41] and [33].

From Eqs.(20),(21),(25),(26); we obtain that

$$D < 1 : \quad H_{3,\text{in}} < H_{2,\text{in}} < H_{3,\text{stag}} < H_{2,\text{stag}} < H_1, \quad (27)$$

$$D > 1 : \quad H_{3,\text{in}} < H_{2,\text{in}} < H_1 < H_{3,\text{stag}} < H_{2,\text{stag}}. \quad (28)$$

Specifically, for $D = 0.25$:

$$\begin{aligned} H_1 &= \frac{1}{4} A^2 = 0.25 A^2, \\ H_{2,\text{in}} &= \frac{3}{32} A^2 \approx 0.094 A^2, \quad H_{2,\text{stag}} = \frac{5}{32} A^2 \approx 0.16 A^2, \\ H_{3,\text{in}} &= \frac{7}{128} A^2 \approx 0.055 A^2, \quad H_{3,\text{stag}} = \frac{7}{64} A^2 \approx 0.1 A^2. \end{aligned}$$

Hence H_1 has the highest energy as stated in Eq.(27). For large H at fixed A , the dynamics select the constrained maximizer, i.e., the 1-site state for $D < 1$ [33], consistent with our $a_\ell(t)$ results (see Figs. 4, 6).

Setting $D = 2$ in Eqs. (20), (21), and (25), we find

$$\begin{aligned} H_1 &= \frac{1}{4} A^2, \quad H_{2,\text{in}} = -\frac{1}{8} A^2, \quad H_{2,\text{stag}} = \frac{3}{8} A^2, \\ H_{3,\text{in}} &= -\frac{7}{44} A^2, \quad H_{3,\text{stag}} = \frac{7}{20} A^2, \end{aligned}$$

where $H_{2,\text{stag}} = 0.375 A^2$ has the highest energy, closely followed by $H_{3,\text{stag}} = 0.35 A^2$, in the order as in Eq.(28). Hence, for $D > 1$, the constrained maximizer in the staggered family is the two-site staggered compacton [33], which dominates at large H for fixed A . It is thus relevant to appreciate that the predominant dynamical observation in the case of $D = 2$ involves such a 2-site staggered configuration, rather than the three-site states which are not generic in this case. Indeed, in our tests the latter appear only when the initial data excite two or more adjacent sites with nearly equal phases (see Eq.(15) as an example initial state used for such observation).

In our computations, corroborating the above energetic calculations, we defined the initial state as $b_\ell = \sqrt{A_\ell} e^{i\ell\pi/2}$ with $A_\ell = a + \epsilon_\ell^c \exp[x\eta_\ell]$ (see Sec. II, Eq. (14) for details), and excited $m = 1, 2, 3, \dots$ neighboring sites (Eq. 15) in the middle of the lattice ($S = \{\ell_0, \dots, \ell_0 + m-1\}$, $\ell_0 = \frac{N}{2} + 2 - m$) as $b_S = \sqrt{A_S} e^{iS\pi/2}$ with a similar amplitude to the other excitations on the lattice, i.e., $A_S = \frac{\max(A_\ell)}{m}$, to mimic a natural occurrence of nearest neighbor excitations.

As we increase D from 0.25 to 2 in our simulations, for a system with a high H/A^2 (i.e., expectedly in the nonergodic regime), the energy of two site solutions $H_{2,\text{stag}} = (1+D)A^2/8$ surpasses the energy of the single site solutions $H_1 = A^2/4$. This happens at $D = 1$; $H_{2,\text{stag}} = H_1 = A^2/4$, and thus for $D > 1$, $H_{2,\text{stag}}$ is favored, consistent with our numerical observations. For $D < 1$, one-site localization occurs in this nonergodic regime, similarly, e.g., to the findings of [20, 21] (for different models). At $D = 1$, we analytically find that one-, two-, and three-site compactons are the energy maximizers: $H_1 = H_2 = H_3 = A^2/4$ (see Appendix B). However, in our simulations at $D = 1$, we mainly observe

one-site localizations. For $D = 1$, two- and three-site localized structures are typically observed only when the initial state is prepared with nearest-neighbor excitations $m = 2, 3$ using Eq. (15). Finally, for $D > 1$, it is instead 2-site staggered localization that we expect to observe in the nonergodic regime.

To illustrate the analytical expectation of one-site localization for $D < 1$ and a two-site staggered compacton for $D > 1$ beyond the examples at $D = 0.25$ and $D = 2$, we show in Fig. 6 two representative nonergodic initial states prepared with Eq. (14) at fixed $a = 0.25$: $(c, x) = (4, 12)$ for $D = 0.75$ and $(c, x) = (10, 18, 13)$ for $D = 1.25$ (chosen to reach the nonergodic regime at each D); cf. Eq. (14). These yield $h = 0.57$ and $h = 1.25$, respectively. For $D = 0.75 < 1$ we observe one-site localization, whereas for $D = 1.25 > 1$ we observe a two-site staggered compacton. These results are consonant with the energy maximizers that are presented in Appendix B. For clarity, we plot only a subset of lattice sites to show the localization structure.

Although the compacton solutions assume vanishing amplitudes outside their support, they still serve as practical guides for the localized standing waves observed in our extended lattice simulations. The 1-, 2-, and 3-site patterns shared here for $D = 0.25$ and $D = 2$ are consistent with the energy orderings given in Eq.(27),(28), and with the analytical results of [32, 33].

IV. DISCUSSION

In summary, the toy model demonstrates thermalization across a broad parameter space, but not all thermalized regions conform to the traditional Gibbs statistical framework. As illustrated in Fig. 1, we observe a parameter region where ergodicity is achieved, although Gibbs statistics fails to describe it accurately. This indicates that non-standard statistics may be required for a comprehensive description. This regime appears to be above the $\beta \rightarrow 0$ line and is consonant (also based on the observations of the nonergodic regime) to a setting of negative temperatures. Furthermore, we confirmed an ergodic-to-nonergodic transition by examining finite-time averages $q(T)$, probability density functions (PDFs), and long-time norm localizations.

As the nonlinear interaction parameter D increases, the parametric regions of different types of behavior are significantly affected. In Fig. 2, the fluctuations of the dimensionless variance $q(T)$ are visually more pronounced at larger D . In the ergodic regimes, the long-time decay crosses over from an initial $\sim T^{-1/2}$ to a faster $\sim T^{-1}$ trend, and this crossover occurs at earlier times for larger D . These observations indicate that stronger nonlinear coupling promotes faster approach to the T^{-1} scaling associated with ergodic dynamics in our diagnostics. Moreover, our simulations suggest that increasing D expands the region of (a, h) parameter space where ergodic — yet, non-Gibbs — behavior is observed (see Fig.1), and

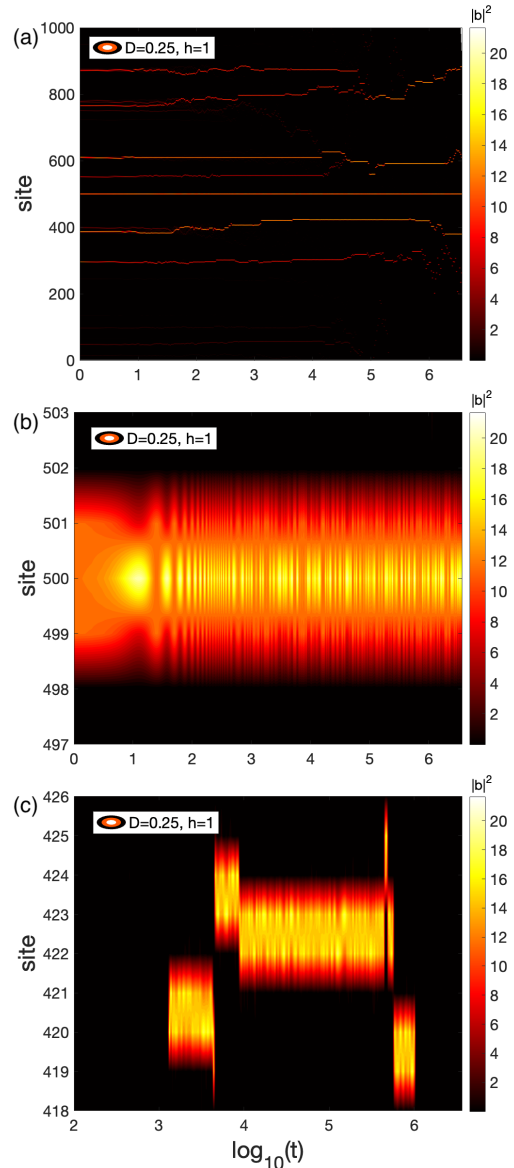


Figure 5. High-energy localization on two and three sites for $D = 2$. Local norm densities a_ℓ are color-coded in time for $a = 0.25, h = 1$. We present the whole lattice in top figure. We zoom to a 3-site, in-phase localization in the middle panel. We zoom to the dominant 2 site staggered localization in bottom. The initial state is prepared according to Eq.(15) setting $a = 0.25, x = 19, c = 21$.

within that region for the same (a, h) parameter set, the crossover to the $\sim T^{-1}$ scaling occurs earlier for larger D .

Fig. 3 shows that, for high energies, the probability distribution of local norms deviates from typical Gaussian behavior, displaying heavy tails. This is indicative of long-lived localized states and suggests that the system does not completely thermalize in the conventional sense. Instead, it exhibits quasi-equilibrium states where persistent nonlinear structures, such as breathers and compactons, dominate the dynamics. This method, with er-

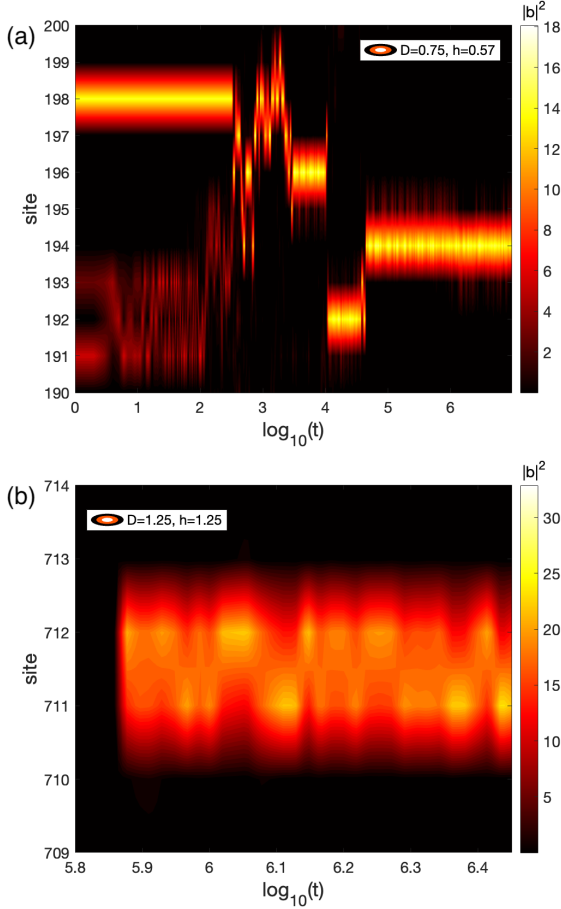


Figure 6. Nonergodic dynamics exhibits a one-site compacton for $D < 1$ and a two-site staggered compacton for $D > 1$. Local norm densities are shown as a function of time for $a = 0.25$: (a) $D = 0.75$, $h = 0.57$ and (b) $D = 1.25$, $h = 1.25$. The initial states are prepared using Eq. (14) with the same random realization of η_ℓ and ϵ_ℓ , using $(c, x) = (4, 12)$ in (a) and $(c, x) = (10, 18.13)$ in (b). For clarity, we plot only a subset of lattice sites (a zoom in ℓ) to highlight the localization pattern.

godicity independently assessed via the variance $q(T)$ and supported by the time evolution of $a_\ell(t)$, allows a clear identification of the ergodic-nonergodic crossover shown in Fig. 1, whereas the other diagnostics considered here do not resolve the crossover as sharply.

To observe how the norm is distributed on the lattice in time, as we progress from an ergodic to a nonergodic system, in Fig. 4, we increase the energy density h of the lattice from (a) 0.02 ($\beta > 0$) to (b) 0.0315 ($\beta = 0$), and to (c) 0.07 ($\beta < 0$); while the norm density $a = 0.25$ and $D = 0.25$ are kept fixed. In Fig. 4(d), we have a closer look to the one-site localization in the case of (c) $h = 0.07$. Note that although it occurs as a yellow dot near $T = 10^8$ on site 938, this is actually a long-time localization on site 938 in between $T = 10^{7.9}$ to $T = 10^8$, which corresponds to a time interval of nearly $2 \cdot 10^7$. It is accordingly evident that single-site localization

dominates the (very) long system evolution dynamics, in line with our discussion of the previous section.

As D increases above 0.5, the Gibbsian thermalization region altogether disappears (in line with the divergence of the TIO). In the latter regime, we observe non-Gibbsian thermalization into states of apparent negative temperature that we infer from alternative diagnostics such as finite time averages or/and excursion time PDF's. In addition to this regime of non-Gibbsian thermalization, for sufficiently strong nonlinearities (large H/A^2), we notice that the system favors persistent localization, overwhelmingly supported on energy maximizers that switch from single site localization for $D < 1$, to two-site (indeed staggered) localization for $D > 1$.

For $D = 0.25$, the system shows predominantly 1-site localization (see Fig. 4), whereas for $D = 2$, we observed 2-site and 3-site stable localization (see Fig. 5). The 2-site (staggered) structures are generically favored, although, as is shown in the figure, an initialization of a 3-site *in-phase* excitation yields a structure that is quite long-lived, suggesting connections with the work of [41] on energy minimizers. These findings are consistent with previous work [33], which identified multi-site compactons in similar nonlinear systems. The behavior of the toy model for different values of D correlates well with the theoretical predictions of localization patterns based on energy maximizers.

V. CONCLUSIONS & FUTURE CHALLENGES

We investigated the statistical properties of a toy model previously derived from the continuum 2d defocusing NLS model as a simplified representation of potential turbulent cascades in the latter. In this effective lattice model where the nodes are not actual physical lattice sites but rather groups of wavenumbers, both ergodic and nonergodic regimes of dynamical behavior were identified through numerical and, where relevant, corroborated via analytical (such as the mode energy analysis) or quasi-analytical (such as the TIO) methods. Our results highlight a triplet of possible regimes, when $D < 0.5$, which gives way to two regimes when $D > 0.5$. The most elemental regime (in line also with earlier studies such as [14, 18, 20, 29]) is that of Gibbsian thermalization, captured by the TIO method in a way that maps dynamic quantities (such as average energy/mass) to thermodynamic ones (such as temperature and chemical potential). A distinct non-Gibbs ergodic region is identified beyond $\beta \rightarrow 0$, characterized by a divergence in excursion times. Furthermore, we demonstrated that the variance of the excursion times exhibits a characteristic power-law decay, transitioning from a $1/\sqrt{T}$ behavior to a $1/T$ decay in thermalized systems. Additionally, when a second transition line to a nonergodic regime is crossed, we observed long-time two-site localization for $D = 2$ in high-energy nonergodic systems, while $D = 0.25$ favored one-site localization. More generally, we fully characterized

this localization and associated it with energy maximizers (evoking an analogy with the work of [41] which refers to energy minimizers) for our effective negative temperature regime. We believe that these findings advance our understanding of thermalization and localization in nonlinear systems and suggest further exploration into energy localization mechanisms and the emergence of compacton states.

Naturally, the above analysis poses a variety of emergent questions regarding the thermodynamic analysis of such nonlinear dynamical lattices. Among them, perhaps predominant remains whether a characterization of the thermodynamics of the apparently ergodic, yet non-Gibbsian regime can be systematically provided, both here, but also in similar models where such phenomenology is obtained [20]. On a related note, the present work, as well as that of [41] presents an interesting characterization of the nonergodic regime as being predominantly centered (in its dynamic characterization) around the energy maximizers (or minimizers). It would be worthwhile to explore whether this is a more generically true feature, especially in models such as the one herein (with competing features) where parametric variations induce a modification of maximizers and hence of the nature of the dynamical localization observations. More generally the theme of statistical mechanics of lattices remains an intriguing nexus of different fields, where the potential inclusion of more conservation laws (when these exist) or the analysis of higher-dimensional systems (when these are physically relevant as, e.g., for the DNLS [14]) are bound to provide numerous future insights.

ACKNOWLEDGMENTS

This work was funded by the Deutsche Forschungsgemeinschaft (DFG, German Research Foundation) – Project-ID 414984028 – SFB 1404 FONDA and supported through the DFG Walter Benjamin Programme (Grant No. 506198590) (Y.K.). We acknowledge support from the Ministry of Science, Technological Development and Innovation of the Republic of Serbia, Grant No. 451-03-136/2025-03/200017 and 451-03-137/2025-03/ 200124. This material is based upon work supported by the US National Science Foundation under Grant No. PHY-2110030, PHY-2408988 and DMS-2204702 (P.G.K.). This research was partly conducted while P.G.K. was visiting the Okinawa Institute of Science and Technology (OIST) through the Theoretical Sciences Visiting Program (TSVP) and the Sydney Mathematical Research Institute (SMRI) of the University of Sydney. This work was also supported by the Simons Foundation [SFI-MPS-SFM-00011048, P.G.K.].

DATA AVAILABILITY

The data supporting the findings of this study are available from the corresponding author upon reasonable request.

Appendix A: Phase Diagram for Toy Model

1. Infinite temperature, $\beta \rightarrow 0$

For the norm density, we have:

$$a = -\frac{1}{\beta N} \frac{\partial \ln Z}{\partial \alpha} = -\frac{1}{\beta \lambda_0} \frac{\partial \lambda_0}{\partial \alpha} \quad (\text{A1})$$

where

$$Z = (2\pi)^N \lambda_0^N, \quad \frac{\partial Z}{\partial \lambda_0} = (2\pi)^N N \lambda_0^{N-1}, \quad (\text{A2})$$

$$\begin{aligned} \frac{\partial \ln Z}{\partial \alpha} &= \frac{1}{Z} \frac{\partial Z}{\partial \alpha} = \frac{1}{Z} \frac{\partial Z}{\partial \lambda_0} \frac{\partial \lambda_0}{\partial \alpha} \\ &= \frac{N}{(2\pi)^N \lambda_0^N} (2\pi)^N \lambda_0^{N-1} \frac{\partial \lambda_0}{\partial \alpha} = \frac{N}{\lambda_0} \frac{\partial \lambda_0}{\partial \alpha}. \end{aligned} \quad (\text{A3})$$

$$\begin{aligned} h &= -\frac{1}{N} \frac{\partial \ln Z}{\partial \beta} + \frac{1}{N} \frac{\alpha}{\beta} \frac{\partial}{\partial \alpha} \ln Z \\ &= -\frac{1}{N} \frac{\partial \ln Z}{\partial \beta} - \alpha a = -\frac{1}{\lambda_0} \frac{\partial \lambda_0}{\partial \beta} - \alpha a, \end{aligned} \quad (\text{A4})$$

where

$$\begin{aligned} \frac{\partial \ln Z}{\partial \beta} &= \frac{1}{Z} \frac{\partial Z}{\partial \beta} = \frac{1}{Z} \frac{\partial Z}{\partial \lambda_0} \frac{\partial \lambda_0}{\partial \beta} \\ &= \frac{1}{(2\pi)^N \lambda_0^N} (2\pi)^N N \lambda_0^{N-1} \frac{\partial \lambda_0}{\partial \beta} = \frac{N}{\lambda_0} \frac{\partial \lambda_0}{\partial \beta}. \end{aligned} \quad (\text{A5})$$

Recalling the partition function of Eq. (6), we write

$$\begin{aligned}
Z &= (2\pi)^N \int_0^\infty \prod_{m=1}^N dA_m I_0 \left[\frac{\beta D}{2} A_m A_{m+1} \right] \\
&\times \exp \left[-\beta \sum_\ell \frac{1}{8} (A_\ell^2 + A_{\ell+1}^2) + \frac{\alpha}{2} (A_\ell + A_{\ell+1}) \right] \\
&= (2\pi)^N \int_0^\infty \prod_{m=1}^N dA_m I_0 \left[\frac{\beta D}{2} A_m A_{m+1} \right] \\
&\times \exp \left[-\beta \sum_\ell \frac{1}{4} |A_\ell|^2 + \alpha A_\ell \right] \\
&= (2\pi)^N \left\{ \int_0^\infty e^{-\beta \alpha A_m} \left[1 - \frac{\beta A_m^2}{4} + \frac{1}{2} \left(\frac{\beta A_m^2}{4} \right)^2 \right] \right. \\
&\times I_0 \left[\frac{\beta D}{2} A_m A_{m+1} \right] dA_m \left. \right\}^N \\
&= (2\pi)^N \left\{ \int_0^\infty e^{-\beta \alpha A_m} \left[1 - \frac{\beta A_m^2}{4} + \frac{1}{2} \left(\frac{\beta A_m^2}{4} \right)^2 \right] dA_m \right\}^N \\
&= (2\pi)^N I(\beta, \alpha)^N, \tag{A6}
\end{aligned}$$

in which we used $I_0 \left[\frac{\beta D}{2} A_m A_{m+1} \right]^N = 1$ for $\beta = 0$, and

$$\begin{aligned}
e^{-\beta(\frac{A^2}{4} + \alpha A)} &= e^{-\beta \alpha A} e^{-\beta A^2/4} \\
&= e^{-\beta \alpha A} \left(1 - \frac{\beta A^2}{4} + \frac{1}{2} \left(\frac{\beta A^2}{4} \right)^2 - \dots \right), \tag{A7}
\end{aligned}$$

$$\prod_m e^{-\beta \alpha A_m} e^{-\beta A_m^2/4} = \prod_m e^{-\beta \alpha A_m} \left(1 - \frac{\beta A_m^2}{4} + \dots \right). \tag{A8}$$

We use the gamma function $\Gamma(n) = (n-1)!$

$$\frac{\Gamma(m+1)}{g^{m+1}} = \int_0^\infty x^m e^{-gx} dx, \tag{A9}$$

$$\int x^2 e^{-gx} dx = \Gamma(3)/(\beta\alpha)^3, \tag{A10}$$

$$\int x^4 e^{-gx} dx = \Gamma(5)/g^5. \tag{A11}$$

To calculate the integral expression $I(\beta, \alpha)$ in Eq.(A6):

$$\begin{aligned}
I &= \int_0^\infty e^{-\beta \alpha A_m} \left(1 - \frac{\beta A_m^2}{4} + \frac{1}{2} \left(\frac{\beta A_m^2}{4} \right)^2 - \dots \right) dA_m \\
&= \int_0^\infty e^{-\beta \alpha A_m} dA_m - \frac{\beta}{4} \int_0^\infty A_m^2 e^{-\beta \alpha A_m} dA_m \\
&\quad + \frac{1}{2} \frac{\beta^2}{16} \int_0^\infty A_m^4 e^{-\beta \alpha A_m} dA_m \\
&= -\frac{1}{\beta \alpha} e^{-\beta \alpha A_m} (0, \infty) - \frac{\beta}{4} \frac{\Gamma(3)}{(\beta\alpha)^3} + \frac{1}{2} \frac{\beta^2}{16} \frac{\Gamma(5)}{(\beta\alpha)^5} \\
&= \frac{1}{\beta \alpha} - \frac{\beta}{4} \frac{2}{(\beta\alpha)^3} + \frac{1}{2} \frac{\beta^2}{16} \frac{4.3.2}{(\beta\alpha)^5} \tag{A12}
\end{aligned}$$

For $\beta = 0, I_0(0) = 1$, then we can simply write Z as

$$\begin{aligned}
Z &= (2\pi)^N I^N = (2\pi)^N \left[\frac{1}{\beta\alpha} - \frac{\beta}{2(\beta\alpha)^3} + \frac{3}{4} \frac{\beta^2}{(\beta\alpha)^5} \dots \right]^N \\
&\approx (2\pi)^N \left(\frac{1}{\beta\alpha} - \frac{\beta}{2(\beta\alpha)^3} \right)^N \\
&= (2\pi)^N \left(\frac{1}{\beta\alpha} \right)^N \left(1 - \frac{1}{2} \frac{\beta}{(\beta\alpha)^2} \right)^N. \tag{A13}
\end{aligned}$$

in which $\beta \rightarrow 0, \alpha \rightarrow \infty, \beta\alpha = \text{const}$. We now take the logarithm to calculate the zero temperature (a, h) :

$$\ln(1-x) = - \sum_{n=1}^\infty \frac{x^n}{n} \approx -x - x^2/2 - x^3/3 \dots \approx -x - x^2/2$$

Thus

$$\ln(1 - \frac{\beta}{2(\beta\alpha)^2}) = -\frac{1}{2\beta\alpha^2} - \frac{1}{8\beta^2\alpha^4}. \tag{A14}$$

$$\begin{aligned}
\ln Z &= N \ln(2\pi) - N \ln(\beta\alpha) + N \ln(1 - \frac{\beta}{2(\beta\alpha)^2}) \\
&\approx N \ln(2\pi) - N \ln(\beta\alpha) - \frac{N}{2\beta\alpha^2} - \frac{N}{8\beta^2\alpha^4} \tag{A15}
\end{aligned}$$

$$\frac{\partial \ln Z}{\partial \alpha} = -\frac{N}{\beta\alpha} \beta - \frac{N}{2\beta} (-2)\alpha^{-3} = -\frac{N}{\alpha} + \frac{N}{\beta\alpha^3} - \frac{N}{2\beta^2\alpha^5} \tag{A16}$$

$$\frac{\partial \ln Z}{\partial \beta} = -\frac{N}{\beta} + \frac{N}{2(\beta\alpha)^2} + \frac{\beta N}{4(\beta\alpha)^4} \tag{A17}$$

Recalling Eq. (10)

$$\begin{aligned}
a &= -\frac{1}{\beta N} \frac{\partial \ln Z}{\partial \alpha} = -\frac{1}{\beta N} \left(-\frac{N}{\alpha} + \frac{N}{\beta\alpha^3} - \frac{N}{2\beta^2\alpha^5} \right) \\
&= \frac{1}{\alpha\beta} - \frac{1}{\beta^2\alpha^3} + \frac{1}{2\beta^3\alpha^5} \underset{\beta \rightarrow 0}{\approx} \frac{1}{\alpha\beta} \tag{A18}
\end{aligned}$$

Recalling Eq. (A4)

$$\begin{aligned}
h &= -\frac{1}{N} \frac{\partial \ln Z}{\partial \beta} - \alpha a \\
&= \left(\frac{1}{\beta} - \frac{1}{2\alpha^2\beta^2} - \frac{1}{4\beta^3\alpha^4} \right) - \alpha \left(\frac{1}{\alpha\beta} - \frac{1}{\beta^2\alpha^3} + \frac{2}{4\beta^3\alpha^5} \right) \\
&= \frac{1}{2\alpha^2\beta^2} - \frac{3\beta}{4(\beta\alpha)^4} \underset{\beta \rightarrow 0}{\approx} \frac{1}{2\alpha^2\beta^2} = \frac{a^2}{2} \tag{A19}
\end{aligned}$$

in which we used

$$\ln Z \approx N \ln(2\pi) - N \ln(\beta\alpha) - \frac{N}{2\alpha^2\beta} \tag{A20}$$

$$\frac{\partial \ln Z}{\partial \beta} = -\frac{N}{\beta} + \frac{N}{2\alpha^2\beta^2}. \tag{A21}$$

We found $h = a^2/2$ in Eq. (A19) for $\beta \rightarrow 0$.

2. Zero temperature ($\beta \rightarrow \infty$)

When the temperature is zero, $\beta \rightarrow \infty$, the minimum energy is realized when all phases keep the same phase difference π such that $\theta_\ell = \ell\pi$, and $A_\ell = a$. This leads to

$$b_\ell = \sqrt{A_\ell} e^{i\theta_\ell} = \sqrt{a} e^{i\ell\pi}, \quad b_\ell^2 = a e^{2i\ell\pi}, \quad (\text{A22})$$

$$b_\ell^{*2} = a e^{-2i\ell\pi} \quad |b_\ell|^4 = a^2 \quad (\text{A23})$$

$$\begin{aligned} b_\ell^{*2} b_{\ell-1}^2 + b_\ell^2 b_{\ell-1}^{*2} &= a^2 e^{-2i\ell\pi+2i(\ell-1)\pi} + a^2 e^{2i\ell\pi-2i(\ell-1)\pi} \\ &= a^2(e^{-2i\pi} + e^{2i\pi}) = 2a^2 \cos(2\pi) = 2a^2 \end{aligned} \quad (\text{A24})$$

Inserting Eq. (A22) and Eq. (A24) into the Hamiltonian Eq. (3) gives

$$\begin{aligned} h &= \frac{H}{N} = \frac{1}{N} \sum_\ell \frac{1}{4} |b_\ell|^4 - \frac{D}{4} (b_\ell^{*2} b_{\ell-1}^2 + b_\ell^2 b_{\ell-1}^{*2}) \\ &= \frac{1}{N} N \left(\frac{a^2}{4} - \frac{D}{4} 2a^2 \right) = \frac{a^2}{4} (1 - 2D) = \frac{a^2}{4} (1 - 2D) \end{aligned} \quad (\text{A25})$$

Appendix B: Staggered compacton solutions for $m = 1-6$

Here we examine the Hamiltonian of different configurations for a fixed norm A .

1 site. $S = \{\ell_0\}$, set $A_{\ell_0} = A$. (The phase is irrelevant since there is no coupling term.)

$$H = \frac{1}{4} A^2, \quad H_1(D) = \frac{1}{4} A^2.$$

2 sites. $S = \{\ell_0, \ell_0 + 1\}$, set $A_{\ell_0} = x$, $A_{\ell_0+1} = y$, with $x + y = A$. For the staggered compacton ($\Delta\phi = \pi/2$),

$$H(x, y) = \frac{1}{4}(x^2 + y^2) - \frac{D}{2}xy \cos(2\Delta\phi) = \frac{1}{4}(x^2 + y^2) + \frac{D}{2}xy.$$

Extremize

$$\mathcal{L}(x, y, \lambda) = \frac{1}{4}(x^2 + y^2) + \frac{D}{2}xy + \lambda(x + y - A),$$

which gives

$$\begin{aligned} \partial_x \mathcal{L} : \quad & \frac{1}{2}x + \frac{D}{2}y + \lambda = 0, \\ \partial_y \mathcal{L} : \quad & \frac{1}{2}y + \frac{D}{2}x + \lambda = 0, \\ & x + y = A. \end{aligned}$$

Solving yields $x = y = A/2$ (for $D \neq 1$), and

$$H_{2,\text{stag}}(D) = \frac{1+D}{8} A^2. \quad (\text{B1})$$

3 sites. $S = \{\ell_0 - 1, \ell_0, \ell_0 + 1\}$, set $A_{\ell_0-1} = A_{\ell_0+1} = x$, $A_{\ell_0} = y$, with $2x + y = A$.

$$H(x, y) = \frac{1}{2}x^2 + \frac{1}{4}y^2 - Dxy \cos(2\Delta\phi).$$

For the staggered compacton ($\Delta\phi = \pi/2$), extremize

$$\mathcal{L}(x, y, \lambda) = \frac{1}{2}x^2 + \frac{1}{4}y^2 + Dxy + \lambda(2x + y - A),$$

which gives the stationarity system

$$\begin{aligned} \partial_x \mathcal{L} : \quad & x + Dy + 2\lambda = 0, \\ \partial_y \mathcal{L} : \quad & \frac{1}{2}y + Dx + \lambda = 0, \\ & 2x + y = A. \end{aligned}$$

Solving yields

$$x = \frac{1-D}{3-4D} A, \quad y = \frac{1-2D}{3-4D} A \quad (D \neq \frac{3}{4}),$$

and the corresponding energy

$$H_{3,\text{stag}}(D) = \frac{1-2D^2}{4(3-4D)} A^2. \quad (\text{B2})$$

4 sites. $S = \{\ell_0 - 1, \ell_0, \ell_0 + 1, \ell_0 + 2\}$, set $A_{\ell_0-1} = A_{\ell_0+2} = x$, $A_{\ell_0} = A_{\ell_0+1} = y$, with $2x + 2y = A$. For the staggered compacton ($\Delta\phi = \pi/2$),

$$\begin{aligned} H(x, y) &= \frac{1}{4}(2x^2 + 2y^2) + \frac{D}{2}(xy + y^2 + yx) \\ &= \frac{1}{2}x^2 + \frac{1}{2}(1+D)y^2 + Dxy. \end{aligned} \quad (\text{B3})$$

Extremize

$$\mathcal{L}(x, y, \lambda) = \frac{1}{2}x^2 + \frac{1}{2}(1+D)y^2 + Dxy + \lambda(2x + 2y - A),$$

which gives

$$\begin{aligned} \partial_x \mathcal{L} : \quad & x + Dy + 2\lambda = 0, \\ \partial_y \mathcal{L} : \quad & (1+D)y + Dx + 2\lambda = 0, \\ & 2x + 2y = A. \end{aligned}$$

Solving yields (for $D \neq 2$)

$$x = \frac{1}{2(2-D)} A, \quad y = \frac{1-D}{2(2-D)} A,$$

and the corresponding energy

$$H_{4,\text{stag}}(D) = \frac{1+D-D^2}{8(2-D)} A^2. \quad (\text{B4})$$

5 sites. $S = \{\ell_0 - 2, \ell_0 - 1, \ell_0, \ell_0 + 1, \ell_0 + 2\}$, set $A_{\ell_0\pm 2} = x$, $A_{\ell_0\pm 1} = y$, $A_{\ell_0} = z$, with $2x + 2y + z = A$. For the staggered compacton ($\Delta\phi = \pi/2$),

$$\begin{aligned} H(x, y, z) &= \frac{1}{4}(2x^2 + 2y^2 + z^2) + \frac{D}{2}(xy + yz + zy + yx) \\ &= \frac{1}{2}x^2 + \frac{1}{2}y^2 + \frac{1}{4}z^2 + D(xy + yz). \end{aligned} \quad (\text{B5})$$

Extremize $\mathcal{L} = H + \lambda(2x + 2y + z - A)$, yielding

$$\begin{aligned}\partial_x \mathcal{L} : \quad & x + Dy + 2\lambda = 0, \\ \partial_y \mathcal{L} : \quad & y + D(x + z) + 2\lambda = 0, \\ \partial_z \mathcal{L} : \quad & \frac{1}{2}z + Dy + \lambda = 0, \\ & 2x + 2y + z = A.\end{aligned}$$

Solving (for $D^2 + 2D - 3 \neq 0$) gives

$$x = \frac{D^2 + D - 1}{D^2 + 8D - 5} A, y = \frac{(2D - 1)A}{D^2 + 8D - 5}, z = \frac{-D^2 + 2D - 1}{D^2 + 8D - 5} A,$$

and

$$H_{5,\text{stag}}(D) = \frac{3D^2 - 1}{4(D^2 + 8D - 5)} A^2. \quad (\text{B6})$$

6 sites. $S = \{\ell_0 - 2, \ell_0 - 1, \ell_0, \ell_0 + 1, \ell_0 + 2, \ell_0 + 3\}$, set $A_{\ell_0-2} = A_{\ell_0+3} = x$, $A_{\ell_0-1} = A_{\ell_0+2} = y$, and $A_{\ell_0} = A_{\ell_0+1} = z$, with $2x + 2y + 2z = A$. For the staggered compacton ($\Delta\phi = \pi/2$),

$$\begin{aligned}H(x, y, z) &= \frac{1}{2}(x^2 + y^2 + z^2) + \frac{D}{2}(xy + yz + z^2 + zy + yx) \\ &= \frac{x^2}{2} + \frac{y^2}{2} + (1 + D)\frac{z^2}{2} + D(xy + yz).\end{aligned} \quad (\text{B7})$$

Extremize $\mathcal{L} = H + \lambda(2x + 2y + 2z - A)$, yielding

$$\begin{aligned}\partial_x \mathcal{L} : \quad & x + Dy + 2\lambda = 0, \\ \partial_y \mathcal{L} : \quad & y + D(x + z) + 2\lambda = 0, \\ \partial_z \mathcal{L} : \quad & (1 + D)z + Dy + 2\lambda = 0, \\ & 2x + 2y + 2z = A.\end{aligned}$$

Solving (for $2D^2 + 2D - 3 \neq 0$) gives

$$\begin{aligned}x &= \frac{(D^2 - 1)A}{2(2D^2 + 2D - 3)}, y = \frac{(D^2 + D - 1)A}{2(2D^2 + 2D - 3)}, \\ z &= \frac{(D - 1)A}{2(2D^2 + 2D - 3)},\end{aligned} \quad (\text{B8})$$

and

$$H_{6,\text{stag}}(D) = \frac{D^3 + 2D^2 - D - 1}{8(2D^2 + 2D - 3)} A^2. \quad (\text{B9})$$

The above stationary solutions are relevant when the resulting amplitudes are nonnegative. The key entry in the Table I that follows is the one with the highest energy (i.e., the energy maximizer). By comparing the row elements, it is straightforward to reach the conclusion reported in the main text. I.e., the maximizer corresponds to the single site for $D < 1$, and to the staggered 2-site state for $D > 1$.

Table I. Coefficients $c_m(D)$ defined by $H_{m,\text{stag}}(D) = c_m(D) A^2$ for $m = 1, \dots, 6$.

D	c_1	c_2	c_3	c_4	c_5	c_6
0.25	0.25	0.156	0.109	0.085	0.069	0.058
0.50	0.25	0.187	0.125	0.104	0.0833	0.0729
0.75	0.25	0.219	—	0.119	0.110	0.0677
1.00	0.25	0.25	0.25	0.125	0.125	0.125
1.25	0.25	0.281	0.266	0.115	0.140	0.135
1.50	0.25	0.312	0.292	0.0625	0.155	0.149
1.75	0.25	0.344	0.320	-0.156	0.170	0.165
2.00	0.25	0.375	0.35	—	0.183	0.181

“—” denotes a singular coefficient due to a zero denominator.

[1] F. Lederer, G. I. Stegeman, D. N. Christodoulides, G. Assanto, M. Segev, and Y. Silberberg, *Physics Reports* **463**, 1 (2008).

[2] O. Morsch and M. Oberthaler, *Rev. Mod. Phys.* **78**, 179 (2006).

[3] V. Nesterenko, *Dynamics of Heterogeneous Materials* (Springer-Verlag, New York, 2001).

[4] Y. Starosvetsky, K. Jayaprakash, M. A. Hasan, and A. Vakakis, *Topics on the Nonlinear Dynamics and Acoustics of Ordered Granular Media* (World Scientific, Singapore, 2017).

[5] M. Sato, B. E. Hubbard, and A. J. Sievers, *Rev. Mod. Phys.* **78**, 137 (2006).

[6] M. Remoissenet, *Waves Called Solitons* (Springer-Verlag, Berlin, 1999).

[7] M. Peyrard, *Nonlinearity* **17**, R1 (2004).

[8] T. Dauxois and M. Peyrard, *Physics of solitons* (Cambridge University Press, Cambridge, 2006).

[9] S. Aubry, *Physica D* **216**, 1 (2006).

[10] S. Flach and A. V. Gorbach, *Physics Reports* **467**, 1 (2008).

[11] C. Chong and P. G. Kevrekidis, *Coherent Structures in Granular Crystals: From Experiment and Modelling to Computation and Mathematical Analysis*, 1st ed. (Springer International Publishing, 2018).

[12] J. C. Eilbeck and M. Johansson, Localization and Energy Transfer in Nonlinear Systems , pp. 44 (2003).

[13] M. Ablowitz, B. Prinari, and A. Trubatch, *Discrete and Continuous Nonlinear Schrödinger Systems* (Cambridge University Press, Cambridge, 2004).

[14] P. Kevrekidis, *The discrete nonlinear Schrödinger Equation*, 1st ed. (Springer-Verlag, Heidelberg, 2009).

[15] R. Cruickshank, F. Lorenzi, A. La Rooij, E. F. Kerr, T. Hilker, S. Kuhr, L. Salasnich, and E. Haller, *Phys. Rev. Lett.* **135**, 263404 (2025).

[16] E. Fermi, P. Pasta, S. Ulam, and M. Tsingou, *Studies of the nonlinear problems*, Tech. Rep. (Los Alamos National Laboratory (LANL), Los Alamos, NM (United States), 1955).

[17] M. A. Porter, N. J. Zabusky, B. Hu, and D. K. Campbell, *American Scientist* **97**, 214 (2009).

[18] K. O. Rasmussen, T. Cretegny, P. G. Kevrekidis, and

N. Grønbech-Jensen, *Phys. Rev. Lett.* **84**, 3740 (2000).

[19] S. Iubini, R. Franzosi, R. Livi, G.-L. Oppo, and A. Politi, *New Journal of Physics* **15**, 023032 (2013).

[20] T. Mithun, Y. Kati, C. Danieli, and S. Flach, *Phys. Rev. Lett.* **120**, 184101 (2018).

[21] T. Mithun, C. Danieli, Y. Kati, and S. Flach, *Phys. Rev. Lett.* **122**, 054102 (2019).

[22] C. Danieli, T. Mithun, Y. Kati, D. K. Campbell, and S. Flach, *Phys. Rev. E* **100**, 032217 (2019).

[23] Y. Kati, X. Yu, and S. Flach, *SciPost Phys. Core* **3**, 006 (2020).

[24] Y. Kati, M. V. Fistul, A. Y. Cherny, and S. Flach, *Phys. Rev. A* **104**, 053307 (2021).

[25] M. Malishava and S. Flach, *Chaos: An Interdisciplinary Journal of Nonlinear Science* **32**, 063113 (2022).

[26] F. O. Wu, A. U. Hassan, and D. N. Christodoulides, *Nature Photonics* **13**, 776 (2019).

[27] N. K. Efremidis and D. N. Christodoulides, *Communications Physics* **5**, 286 (2022).

[28] K. G. Makris, F. O. Wu, P. S. Jung, and D. N. Christodoulides, *Optics Letters* **45**, 1651 (2020).

[29] M. Baldovin, S. Iubini, R. Livi, and A. Vulpiani, *Physics Reports* **923**, 1 (2021), statistical mechanics of systems with negative temperature.

[30] S. Iubini and A. Politi, *Physical Review Letters* **134**, 097102 (2025).

[31] J. Colliander, M. Keel, G. Staffilani, H. Takaoka, and T. Tao, *Inventiones mathematicae* **181**, 39 (2010).

[32] J. E. Colliander, J. L. Marzuola, T. Oh, and G. Simpson, *Experimental Mathematics* **22**, 250 (2013), <https://doi.org/10.1080/10586458.2013.793110>.

[33] R. Parker, P. Germain, J. Cuevas-Maraver, A. Aceves, and P. Kevrekidis, *Physica D: Nonlinear Phenomena* **467**, 134273 (2024).

[34] A. D. Jones, G. Simpson, and W. Wilson, *Journal of Computational and Applied Mathematics* **325**, 113 (2017).

[35] S. Herr and J. Marzuola, *Indiana Univ. Math. J.* **65**, 753 (2016).

[36] T. Mithun, A. Maluckov, B. M. Manda, C. Skokos, A. Bishop, A. Saxena, A. Khare, and P. G. Kevrekidis, *Phys. Rev. E* **103**, 032211 (2021).

[37] M. Salerno, *Physical Review A* **46**, 6856 (1992).

[38] D. J. Scalapino, M. Sears, and R. A. Ferrell, *Phys. Rev. B* **6**, 3409 (1972).

[39] P. G. Kevrekidis and V. V. Konotop, *Phys. Rev. E* **65**, 066614 (2002).

[40] P. G. Kevrekidis, V. V. Konotop, A. R. Bishop, and S. Takeno, *Journal of Physics A: Mathematical and General* **35**, L641 (2002).

[41] J. L. Marzuola and J. C. Mattingly, [arXiv:2510.22090](https://arxiv.org/abs/2510.22090) (2025), preprint, [arXiv:2510.22090 \[math.CA\]](https://arxiv.org/abs/2510.22090).

[42] J. A. Krumhansl and J. R. Schrieffer, *Phys. Rev. B* **11**, 3535 (1975).

[43] P. Talkner and P. Hänggi, *Rev. Mod. Phys.* **92**, 041002 (2020).

[44] S. L. Adler, *Quantum theory as an emergent phenomenon: The statistical mechanics of matrix models as the precursor of quantum field theory* (Cambridge University Press, 2004).

[45] C. Danieli, D. K. Campbell, and S. Flach, *Phys. Rev. E* **95**, 060202 (2017).